Kinetics of methane combustion on model supported Pd/LaxMnO3 natural gas vehicle catalysts: Sensitivity of La-stoichiometry on the catalytic properties of Pd

Yuanshuang Zheng, Maya Marinova, Pascal Granger

Submitted to the Chemical Engineering Journal

Revised version manuscript ID: CEJ-D-23-16572

Kinetics of methane combustion on model supported Pd/La_xMnO_3 natural gas vehicle catalysts : Sensitivity of La-stoichiometry on the catalytic properties of Pd.

Yuanshuang Zheng,[1] Maya Marinova,[2] Pascal Granger[1]*

[1] *Univ. Lille, CNRS, Centrale Lille, ENSCL, Univ. Artois, UMR 8181 - UCCS - Unité de Catalyse et Chimie du Solide, F-59000 Lille, France*
[2] *Univ. Lille, CNRS, INRAE, Centrale Lille, Univ. Artois, FR 2638, IMEC - Institut Michel-Eugène Chevreul, F-59000, Lille, France*

Corresponding author : Email : pascal.granger@univ-lille.fr
Phone number : +33 320 434 938

Abstract

The kinetics of the catalytic CH_4/O_2 reaction has been studied on 1 wt.% Pd/La_xMnO_3 with x = 0.7, 1.0 and 1.3. Steady-state kinetic measurements have been performed in lean conditions at 400°C on pre-reduced and on aged catalysts after exposure to wet atmosphere at 750°C. A single site reaction mechanism occurs preferentially on $Pd/La_{1.3}MnO_3$ exhibiting a La-rich surface. In contrast a dual-site reaction mechanism, combining Pd and surface reactive oxygen species from the support, is preferentially involved on $Pd\text{-}La_{0.7}MnO_3$ characterized by a Mn-rich surface. $Pd/LaMnO_3$ exhibits a mixed regime but subsequent deterioration of the $Pd\text{-}La_xMnO_3$ interface during thermal aging leads to increasing contribution of the single site reaction mechanism. High surface Pd/Mn ratio and high concentration of Pd^{n+} with n > 2 can be considered as good descriptors to probe the efficacy of Pd/La_xMnO_3 catalysts. Remarkably, the high thermal stability of the $Pd\text{-}La_{0.7}MnO_3$ interface, preserving the Pd dispersion on $Pd/La_{0.7}MnO_3$, leads to lower sensitivity to deactivation.

Keywords: Methane combustion, post-combustion catalysis, Palladium, perovskite, kinetics

1. Introduction

Natural gas is recognized as an alternative to liquid Diesel and gasoline fuels. Compressed Natural Gas (CNG) vehicles are less harmful toward environment with lower particulates and NO_x emissions [1]. However, particular attention must be paid towards CH_4 emissions control because of its higher global warming power compared to CO_2, nearly 20 times higher. Catalytic after-treatment technologies are currently implemented to combust traces of methane emitted from the exhaust [2,3]. They contain high total loadings of Platinum Group Metals (PGM) >200 g ft^{-3} to overcome the high chemical stability of methane at high temperature and reduce the deleterious effects of particle sintering that leads to deactivation. Supported palladium catalysts are recognized as benchmark for the CH_4/O_2 reaction. Most of investigations have been performed in lean conditions and concluded that PdO acts as active phase. Particle size effect on the reaction rate was previously observed on Pd/Al_2O_3 with improved Turn-Over-Frequency (TOF) on larger Pd particles [4-6]. In fact, such structure-sensitivity has been related to a stronger stability of the Pd-O bond on small PdO particles. Support effects have been previously discussed in terms of acid-base properties but no clear consensus seems to appear. Indeed, a detrimental impact on the catalytic activity has been reported when palladium cluster anions are stabilized on a basic support [7]. On the contrary, the basic properties of rare earths, led to significant catalytic enhancement ascribed to improved oxygen mobility and higher concentration of surface anionic vacancies that would stabilize PdO at high temperature [8].

The kinetics of catalytic methane combustion has been originally studied on Pd supported on materials developing low oxygen storage properties. As aforementioned, the prominent role of PdO_x was pointed out [9,10]. Still today, the microkinetic approaches from DFT calculations agree with the superiority of PdO (101) characterized by lower dissociative adsorption barrier of methane [11]. Stolz et al. [12] provided interesting mechanistic insights on model PdO (101)

surface with methane dissociation on a Pd_{cus}-O_{cus} site pair. However, the discussion on the architecture of active sites over polycrystalline supported catalysts is still under debate regarding the role of the support material, acting as supplier of reactive oxygen species [13], as well as the oxidation state of active palladium species in the course of the reaction [14,15].

In fact, Alifanti et al. have opened the debate on the role of oxygen mobility on lanthanum-based perovskites involving both reactive suprafacial and intrafacial oxygen species [16]. These authors suggested that compensation effects can be expected when the catalyst is exposed at high temperature as the deterioration surface oxygen mobility, due to the loss of specific surface area, can be partly compensated by a faster bulk oxygen diffusion thanks to improved crystallinity. Spinicci et al. [17] found improved performances in methane conversion on Mn-deficient $LaMn_{0.9}O_3$ composition compared to stoichiometric and La-deficient structures related to less bonded β-lattice oxygen. Interestingly, a gain in three-way catalytic performances has been also observed on Mn-rich $LaMn_{1.2}O_{3+\delta}$ structure ascribed to the segregation of amorphous or small MnO_x crystallites characterized by lower cation vacancies and enhanced oxygen vacancies [18]. Improved oxidative properties have been also evidenced on La-deficient La_xMnO_3 compositions in NO oxidation related to a faster regeneration of reactive oxygen species in connection with greater extent of Mn^{4+} species [19]. Onrubia-Calvo et al. did not found correlation neither with Mn^{4+} nor with the specific surface area on Sr-doped manganite perovskites for the same catalytic application. These authors preferentially ascribed rate-enhancement in NO oxidation to an increase in surface reactive oxygen species [20]. Despite, different catalytic applications, illustrated in these two latter examples, a relative consensus appears emphasizing the conjunction of Mn^{4+} and surface reactive lattice oxygen species in defining optimal catalytic properties for oxidation reactions.

Recent studies on pre-reduced $Pd/La_{0.7}MnO_3$ catalyst in the CH_4/O_2 reaction found that the Pd-perovskite interface governs the kinetics which can be reasonably model by a dual site

reaction mechanism illustrated in scheme 1(b) [21]. According to this mechanism proposal, reactive oxygen species, *i.e.* 'O', would be supplied preferentially by the support material exhibiting oxygen storage properties. However, a high sensitivity of this interface was also observed depending on the inlet gas composition. The effect of water on the kinetics is closely related to the nature of the reaction. Indeed, water chemisorption on Pd/Al_2O_3 enhances CO oxidation thanks to the stabilization of highly-dispersed oxidic Pd species [22]. Conversely, water exposure induces a loss of performance of supported Pd catalysts on perovskite in methane oxidation [21]. In this specific case, the deterioration of the Pd-support interface occurs and induce changes in reaction mechanism with the restoration of a single-site reaction mechanism involving only Pd in the composition of the active phase (see scheme 1(a)). Such a sensitivity can be also related to the catalyst composition as already emphasized on Pd/Al_2O_3-CeO_2 for methane oxidation. Indeed, two kinetic regimes coexist involving both the Pd^0-Ce and Pd^0-PdO interfaces. The prevalence of one over the other is closely related to the size of the PdO particles [13]. Previous studies [15] also reported sharp structural changes driven by the temperature inducing both changes in the oxidation state of Pd, shifting from oxidic to metallic form, and phase transition of the perovskite creating new interface leading to improved methane conversion.

(a)

(1) $O_2(g) + 2* \leftrightarrows 2O*$
(2) $CH_4(g) + * \leftrightarrows CH_4*$
(3a) $CH_4* + O* \rightarrow CH_3* + OH*$
(4a) $CH_3* + O* \rightarrow CH_2* + OH*$
(5a) $CH_2* + O* \rightarrow CH* + OH*$
(6a) $CH* + O* \rightarrow C* + OH*$
(7) $C* + O* \rightarrow CO* + *$
(8) $CO* + O* \rightarrow CO_2(g) + 2*$
(9) $2OH* \rightarrow H_2O(g) + O* + *$

(b)

(1) $O_2(g) + 2* \leftrightarrows 2O*$
(2) $CH_4(g) + * \leftrightarrows CH_4*$
(3b) $CH_4* + $ 'O' $\rightarrow CH_3* +$ 'OH'
(4b) $CH_3* + $ 'O' $\rightarrow CH_2* +$ 'OH'
(5b) $CH_2* + $ 'O' $\rightarrow CH* +$ 'OH'
(6b) $CH* + $ 'O' $\rightarrow C* +$ 'OH'
(7) $C* + O* \rightarrow CO* + *$
(8) $CO* + O* \rightarrow CO_2(g) + 2*$
(10) 2 'OH' $\rightarrow H_2O(g) +$ 'O'

Scheme 1. Single site **(a)** vs. dual site reaction mechanism **(b)** earlier suggested on $Pd/La_{0.7}MnO_3$ catalysts for the CH_4/O_2 reaction [21]. * stands for a palladium adsorption site. 'O' stands for surface reactive oxygen species produced from the perovskite and/or PdO lattice.

In this study, the consequences of changes in lanthanum stoichiometry on the kinetics of the CH_4/O_2 reaction in supported Pd/La_xMnO_3 catalysts have been investigated and discussed based on the comparisons of single or dual site reaction mechanism displayed in scheme 1. In fact, both reaction mechanisms reflect the extent of $Pd\text{-}La_xMnO_3$ interface from weak to strong metal-support interaction. Particular attention was paid to the impact of thermal aging on the stability of the $Pd\text{-}La_xMnO_3$ interface and the consequences on the kinetics.

2. Experimental

2.1. Catalyst preparation and related physicochemical characterization

La_xMnO_3 perovskites were synthesized based on a *citric* route adapted from the sol-gel method earlier described [23]. The different steps for the perovskite synthesis are resumed in Scheme S1 in Supplementary Information (SI). In brief, the experimental protocol consisted in the dissolution of nitrate precursor salts supplied by Sigma Aldrich, *i.e.* $La(NO_3)_3{\cdot}6H_2O$ and $Mn(NO_3)_2{\cdot}4H_2O$, in deionized water. Citric acid (CA) was added to the obtained solution with adjusted concentration to fulfill the following conditions: CA/La+Mn+Pd = 1. Afterward, the solvent was evaporated at 60°C under reduced pressure till obtaining a viscous gel. The gel was dried in static air conditions at 80°C. Prior to calcination in air at 600°C for 8h, the exothermic decomposition of nitrates proceeded in static conditions at 300°C. Palladium was dispersed onto the perovskite support according to a wet impregnation method in an excess of solvent with adjusted amount of palladium nitrate to ultimately get 1 wt.% Pd composition. The impregnated precursors were dried in air at 80°C and then calcined under airflow for 8h at 400°C. The samples were respectively labelled Pt/La_xMnO_3 with x = 0.7, 1.0 and 1.3.

Powder X-ray diffractograms were recorded on a Bruker AXS D8 advance diffractometer in Bragg-Brentanamo geometry fitted with a LynxEye Super Speed detector in the following operating conditions: Cu Kα radiation (λ = 0.154 nm, 40 kV, 30 mA), in a 2θ range 10º-80º with a 2θ step of 0.02º. The reducibility of calcined catalysts was studied from hydrogen temperature-programmed-reduction (H_2-TPR) experiments in a Micromeritics AutoChem II 2920 apparatus. 50 mg of catalyst were exposed to 5 vol.% hydrogen diluted in argon from room temperature (RT) to 1000°C with a constant heating rate dT/dt = 10 ºC min^{-1}. Outlet H_2 concentration was measured thanks to a thermal conductivity detector. Oxygen-Temperature-Programmed Desorption (O_2-TPD) experiments were conducted in the same Micromeritics AutoChem II 2920 apparatus on 50 mg catalyst samples preliminary heated under pure oxygen flow (5 mL/min) at 600°C for 1 hour. After cooling down at RT, the catalyst was progressively heated (dT/dt = 10 °C/min) under helium flow up 1000°C. The concentration of gaseous oxygen released from the sample was monitored by gas chromatography and mass spectrometry (m/z = 32).

The high-resolution scanning transmission electron microscopy (HR-STEM) was carried out on a ThermoFisher Scientific TITAN Themis 300 microscope equipped with high brightness Schottky field effect gun and a probe aberration corrector. Chemical mapping from Scanning Transmission Electron Microscopy coupled to Energy Dispersive Spectroscopy analysis (STEM-EDS) used a super-X windowless 4 quadrant silicon drift detector. STEM observations were carried out with an accelerating voltage of 300 kV, a spot size of about 500 pm, semi-convergence angle of 18 mrad and probe current of approximately 100 pA. High angle annular dark field (HAADF) images were recorded with collection angles in the range 50-200 mrad. STEM-EDS mapping was performed with dwell time of 15 μs per pixel with continuous scanning over multiple frames for a total time of 10−15 min per acquisition.

Nitrogen physisorption isotherms were recorded at -196°C on a Micromeritics Tristar analyser. The samples were outgassed under vacuum for 4 h at 200°C. Specific surface area (SSA) and pore size distribution were respectively calculated according the Brunauer-Emmett-Teller (BET) theory and the Barret-Joyner-Halenda (BJH) theory. XPS surface analysis was performed on a Kratos Axis Ultra spectrometer equipped with a monochromatized Al Kα source (15 mA, 14 KV) and a charge compensation gun. The binding energy (B.E.) of the C 1s core level at 285.0 eV served as internal reference for the determination of B.E. values for Pd 3d, Mn 2p, O 1s and La 3d core levels. The scientific software CasaXPS was used for semiquantitative analysis. The deconvolution of XPS photopeaks took a Gaussian to Lorentzian contribution of 70/30 into account.

2.3. Steady-state and transient catalytic measurements

Steady-state kinetic measurements were performed on a high-throughput Flowrence unit supplied by Avantium. 16 parallel quartz fixed-bed microreactors contained 30 mg catalyst in powder form with an average grain size of 100 μm. The inlet gas mixture was composed of 750-3000 ppm CH_4 with 5 vol.% O_2 in the presence or in the absence of 10 vol.% H_2O in the temperature range 350-600°C. The space velocity for each reactor was kept constant at 60 $L.h^{-1}.g^{-1}$. The outlet gas mixture from each reactor was analyzed by using an Agilent 7890 gas chromatograph. Before kinetic measurements, the catalyst samples were pre-reduced in pure hydrogen at 250°C to reduce PdO to metallic Pd particles. It was previously observed that the rhombohedral structure of the perovskite was insensitive to this pre-reductive treatment [21]. Two series were performed according to the same protocol on pre-reduced samples and then on aged samples after exposure at 750°C for 4h under a gas mixture composed of 5 vol% O_2 and 10 vol.% H_2O. The occurrence of mass transfer phenomena was previously checked through

the calculation of the Weisz-Prater criterion according to Eq. (11) where r_{obs}, stands for the measured reaction rate in mol.m^3.s^{-1}, C_{obs} the residual concentration of methane in the gas phase in mol.m^{-3}, D_{eff,CH_4} the effective diffusivity of CH_4 in m^2.s^{-1}, and L the characteristic length corresponding to the volume to surface ratio in m. The boundary conditions given by Eq. (11) were always verified for CH_4 conversion lower than 10% [21].

$$\frac{r_{obs}L^2}{C_{obs}D_{eff,CH_4}} < 1 \qquad (11)$$

3. Results

3.1. Steady-state kinetic study of the catalytic CH_4/O_2 reaction on Pd/La_xMnO_3 : Impact of La-stoichiometry and thermal aging.

The partial pressure effect on the reaction rate was studied on pre-reduced and aged samples at the same temperature of 400°C. The partial pressure of oxygen $p(O_2)$ was kept constant while for methane $p(CH_4)$ varied in the range (0.75-3.0)×10^{-3} atm. Part of the results are summarized in Table 1. A positive reaction order for methane is obtained in agreement with earlier studies [24,25]. The specific reaction rates measured in dry conditions on pre-reduced and aged catalysts with $p(CH_4)$ = 1.0×10^{-3} atm are comparable on Pd/$La_{0.7}MnO_3$ reflecting a high resistance to thermal aging. A slight deactivation appears on Pd/$LaMnO_3$. In contrast, thermal aging has a significant detrimental effect on the catalytic activity of Pd/$La_{1.3}MnO_3$. It is noticeable that the significant changes in Pd dispersion on pre-reduced catalysts has only a weak influence as the specific reaction rates on pre-reduced Pd/La_xMnO_3 are rather comparable

with deviations likely within the margin of error. This comparison suggests that active sites would not be only composed of palladium atoms.

A decrease in the reaction rate is noticeable in the presence of 0.1 atm. H_2O, affecting equally pre-reduced and aged catalysts. A previous study evidenced that chemisorbed hydroxyl species coming from the dissociation of methane onto PdO can exhibit a longer residence time at low temperature [26]. This effect can be more pronounced especially in the presence H_2O with a much faster water dissociative adsorption on palladium. Such usual inhibiting effect of water on the reaction rate has been described elsewhere [24,25].

The influence of the temperature was studied in the range 250-400°C for pre-reduced catalysts and 400-500°C for aged catalysts with fixed $p(CH_4) = 1.0\times10^{-3}$ atm and $p(O_2) = 5.0\times10^{-2}$ atm. The apparent activation energy E_{app} and the pre-exponential factor A, calculated from the Arrhenius plots (not shown), are compared in Table 1. A previous study observed different kinetic behaviour on Pd^0 and PdO associated to lower activation barrier, *i.e.* 125 kJ/mol vs. 30 kJ/mol respectively, and higher TOF values on PdO making these two experimental kinetic parameters as good descriptors to probe the surface reactivity and related reaction mechanisms for methane combustion [25]. Higher activation barrier on supported calcined Pd/Si-Al_2O_3 catalyst at 85 kJ/mol was reported elsewhere [27]. For metallic Pd (110) exposed to 0.3 vol.% O_2 in the range 590-700°C, the surface would be covered by chemisorbed oxygen but extensive bulk oxidation to PdO was not observed [28]. The order of magnitude obtained for E_{app} on pre-reduced and aged Pd/La_xMnO_3 would rather reflect the behavior of a metallic surface. Interestingly, distinct evolutions on E_{app} and A appear on aged Pd/La_xMnO_3. For $x = 0.7$ and 1, a compensation effect is noticeable with a joint decrease of E_{app} and A values. The lower value of A would reflect a loss in the density of active sites counterbalanced by a lower E_{app} related to either changes in reaction mechanism or alteration of the adsorption properties of palladium sites. On the other hand, no distinct variation appears on these two

parameters calculated on $Pd/La_{1.3}MnO_3$ with marginal deviations likely within the margin of error.

3.2. Structural features vs. reducibility and oxygen mobility of calcined Pd/La_xMnO_3 catalysts

As starting point, physicochemical characterization presented in this section were essentially obtained on calcined catalysts which allowed to examine structural properties in connection with the reducibility of Pd/La_xMnO_3. This latter property is intimated related to changes observed on the oxidation state of oxidic manganese and palladium species. Oxygen mobility is also an important descriptor in determining the potential participation of reactive oxygen species from the perovskite support.

Surface analysis coupled to microscopy analysis were performed both on calcined and aged samples. As a matter of fact, the recovery of low amount of catalyst from high-throughput catalytic testings restricted the investigations of post mortem catalysts. Nonetheless, subsequent comparisons will provide useful information to conduct the discussion and try to establish some relationships between the surface and the catalytic properties as well as their evolution after thermal aging.

3.2.1. Structural properties of calcined Pd/La_xMnO_3 from XRD analysis

Fig. 1 shows XRD diffractograms recorded on calcined Pd/La_xMnO_3. The most intense reflections at 2θ = 32.7°, 47.0°, 58.3° corresponding to the following reflections (110), (024), and (214) are characteristic of the rhombohedral structure of $LaMnO_3$ (PDF 04-012-5560). No discernible shift was observed on their position representative of contraction or expansion of the cell volume. The characteristic peak splitting at 2θ = 32.5° and 32.8° was not observed due to the amorphous character of the samples. Additional weak and broad reflections appear at 2θ

= 36.1° and 59.9° for Pd/$La_{0.7}MnO_3$ which match more with spinel Mn_3O_4 structure (PDF 04-007-1841) highlighting phase segregation. A weak and broad XRD line appears at $2\theta = 29.6°$ assigned to the most intense reflection characteristic of La_2O_3 on calcined Pd/$La_{1.3}MnO_3$.

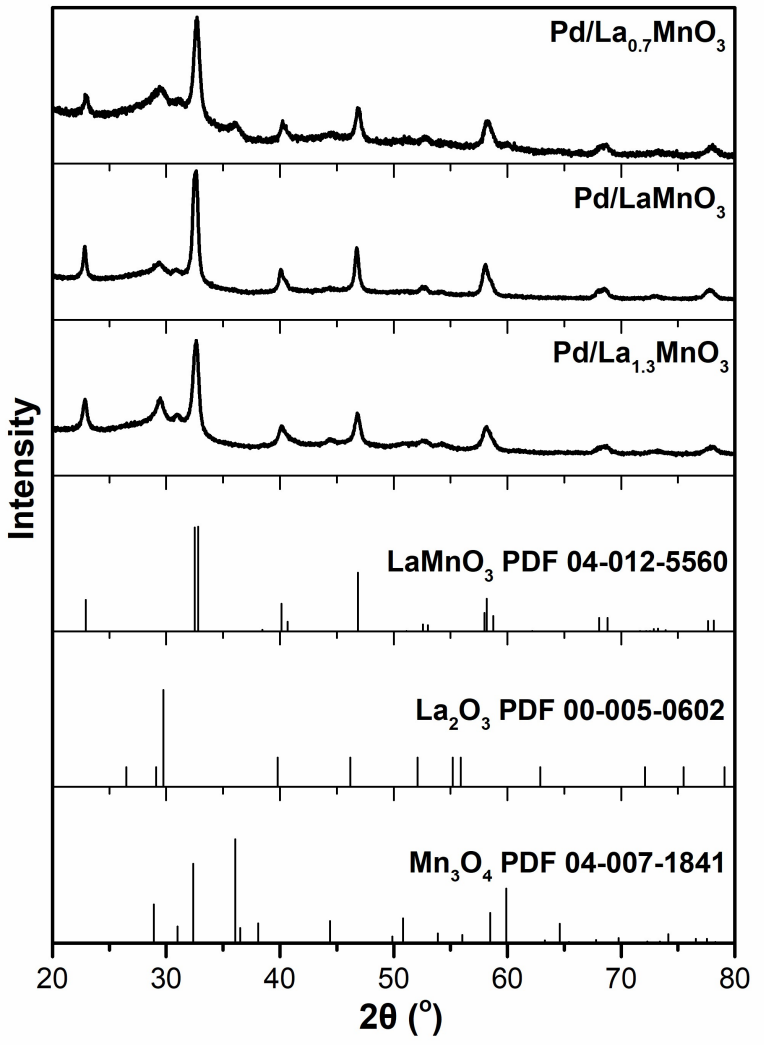

Fig. 1. XRD patterns recorded on calcined Pd/La_xMnO_3.

Table 1. Kinetic parameters for the CH_4/O_2 reaction in lean conditions over pre-reduced and aged Pd-based perovskite catalysts.

Catalyst	Thermal treatment	Pd dispersion (%)	$p(CH_4)$ (10^{-3} atm)	$p(O_2)$ (10^{-3} atm)	$p(H_2O)$ (10^{-3} atm)	Pre-exponential factor, A (s^{-1})[a]	E_{app} (kJ/mol)[a]	CH_4 order	Specif. Rate ($mol.s^{-1}g^{-1}$)[b]	Reference
$Pd/La_{0.7}MnO_3$	Pre-reduced/250°C	6.2	0.75-3.0	50	-	6.2×10^{11}	136.0	0.7	4.5×10^{-8}	[21]
			1	50	100	-	-	-	0.9×10^{-8}	
	Aged		0.75-3.0	50	-	6.4×10^{8}	97.9	0.8	4.4×10^{-8}	
			1	50	100	-	-	-	2.1×10^{-8}	
$Pd/LaMnO_3$	Pre-reduced/250°C	13.0	0.75-3.0	50	-	1.2×10^{8}	140.5	0.7	5.5×10^{-8}	This study
			1	50	100	-	-	-	1.1×10^{-8}	
	Aged		0.75-3.0	50	-	1.8×10^{3}	119.1	n.d.	4.6×10^{-8}	
			1	50	100	-	-	-	1.6×10^{-8}	
$Pd/La_{1.3}MnO_3$	Pre-reduced/250°C	1.0	0.75-3.0	50	-	8.4×10^{6}	127.7	0.7	4.1×10^{-8}	This study
			1	50	100				0.5×10^{-8}	
	Aged		0.75-3.0	50	-	4.5×10^{6}	128.4	n.d.	1.9×10^{-8}	
			1	50	100				0.7×10^{-8}	

[a] with $p(CH_4) = 1.0\times10^{-3}$ atm and $p(O_2) = 50\times10^{-3}$ atm in the temperature range 350-400°C for pre-reduced catalysts and 400-500°C for aged catalysts

[b] T = 400°C $p(CH_4) = 1.0\times10^{-3}$ atm and $p(O_2) = 50\times10^{-3}$ atm

3.2.2. Reducibility of oxidic Mn species: Impact of Pd

H_2-TPR measurements complement these structural observations by analysing the reducibility of oxidic manganese species. Indeed, Mn^{2+} and Mn^{3+} in the spinel structure of Mn_3O_4 can be stabilized respectively in tetrahedral and octahedral coordination. On the other hand, Mn^{4+} and Mn^{3+} can coexist in the perovskite lattice preferentially in octahedral coordination. This agrees with non-stoichiometric $LaMnO_{3+\delta}$ structure stabilized under air conditions with $\delta > 0$ corresponding to Mn^{4+} composition higher than 20% [26,29,30]. As reported, an increase of δ is expected by lowering the sintering temperature. Hence, significant formation of Mn^{4+} is expected on Pd/La_xMnO_3 catalysts with perovskite structure obtained at 600°C. Based on this, a H/Mn ratio higher than 1 should be obtained. An important point is also related to the dispersion of PdO_x species at the surface as subsequent reduction into metallic Pd^0 species can assist the reduction of surface MnO_x species at lower temperature thanks to hydrogen spill-over process.

As seen in Fig. 2, two H_2-consumption ranges appear distinctly on bare $LaMnO_3$ and $La_{1.3}MnO_3$ samples, below and above 600°C, which are consistent with a two-step reduction process $Mn^{4+} \rightarrow Mn^{3+}$ and $Mn^{4+} \rightarrow Mn^{3+}$. Asymmetry on the relative intensity appears on $La_{0.7}MnO_3$ likely due to a greater extent of Mn^{4+}. The H_2-consumption profiles recorded on $Pd/LaMnO_3$ and $Pd/La_{1.3}MnO_3$ do not show drastic changes: A shoulder arises near 200-250°C while a low temperature reduction range arises more distinctly on $Pd/La_{0.7}MnO_3$ below 100°C. These additional contributions can be assigned to the reduction of oxidic palladium species. Jointly, a shift to lower temperature of the Mn^{4+} reduction process on $Pd/La_{0.7}MnO_3$ suggests that metallic Pd species formed at low temperature would ease the reduction of Mn^{4+} species due to the propensity of Pd^0 to adsorb and dissociate hydrogen. The estimates of the H/Mn ratio agree with previous assumptions verifying a higher concentration of Mn^{4+} species especially

on $Pd/La_{0.7}MnO_3$. Such comparisons seem in agreement with significant non-stoichiometry for $LaMnO_{3+\delta}$ composition corresponding to $\delta > 0$ which agrees with a greater stabilization of Mn^{4+} and also underlines a beneficial effect induced by La-deficiency enhancing the formation of Mn^{4+} [29].

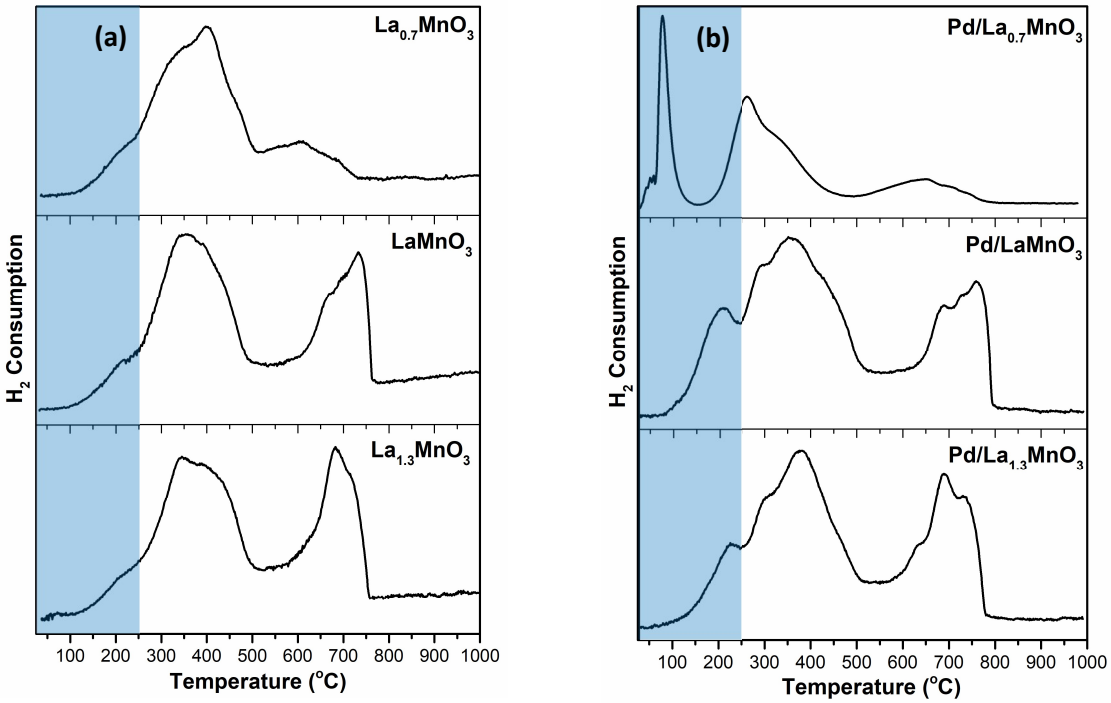

Fig. 2. H_2-consumption profiles vs. temperature from H_2-TPR experiments on bare La_xMnO_3 perovskite materials **(a)** and on calcined Pd-doped perovskite samples **(b)**.

3.2.3. Oxygen-temperature programmed desorption to probe surface and bulk oxygen mobility

Surface and bulk oxygen mobility is a critical parameter which leads previously to the definition of suprafacial or intrafacial reaction mechanisms especially for combustion reactions. O_2-TPD is a powerful technique to distinguish these two processes which differ from the strength of oxygen species bonded to the perovskite at the surface and in the bulk. O_2-desorption profiles are in some extent comparable (see Fig. S1 in SI). A weak desorption takes place below 500°C representative of the desorption of surface oxygen species. This process is *a priori* sensitive to the surface properties, *i.e.* composition and specific surface area [31] and can be

assigned to suprafacial desorption process. Above 500°C a prominent signal appears reflecting bulk oxygen mobility depending on the strength of lattice Mn-O bond associated to intrafacial desorption process. Peak integration led to the estimates of amount of desorbed oxygen in Table 2 showing that the suprafacial oxygen desorption (α-oxygen) is weak and slightly improved in case of non-stoichiometric perovskite compositions. The intensity of the α-oxygen desorption seems consistent with the evolution observed on the specific surface area. The most intense asymmetric signal above 500°C in a broad temperature range can be assigned to intrafacial oxygen desorption (β-oxygen). As observed the strong asymmetry reveals the existence of different contributions likely related to phase segregation previously evidenced from XRD analysis. Quantitative analysis reveals that bulk mobility is improved for $Pd/LaMnO_3$ and this trend is even more accentuated by considering normalized amount of O_2 desorbed expressed per square meter.

3.2.4. HAADF-STEM analysis coupled to EDS

In order to get more insights, HAADF coupled to STEM-EDS analysis was performed to investigate the palladium distribution on calcined samples and check the impact of thermal aging. According to the method used for Pd deposition, palladium should be distributed at the surface. The final calcination at 400°C should not induce significant bulk diffusion inside the perovskite lattice. Main information concerns the evolution of the particle size of palladium before and after aging as well as change in the Mn and La composition. The intensity signal and high resolution in HAADF images depends on the thickness, density and the atomic number $Z^{1.7}$. HAADF images and STEM-EDS maps are collected and compared in Figs. 3-5. On calcined $Pd/La_{0.7}MnO_3$ (Fig. 3), the size of PdO particles varies in the range 1.5-8 nm. Hence, they are in some extent small but often agglomerated PdO particles. The measured interplanar spacing around 2.6 Å emphasizes the prevalence of (101) facets of PdO. The La/Mn ratio is

somewhat a relevant descriptor as it can modulate the strength Pd-$LaMnO_3$ interaction in case of surface gradient concentration of manganese. The spatial distribution of Mn and La has been controlled in different regions on the La-deficient Pd/$La_{0.7}MnO_3$ with sizes varying from 10 nm×10 nm ×100 nm to 200 nm × 200 nm × 100 nm (see Fig 6). For the calcined sample, a broad distribution, over ~70 measurements, is obtained with an average La/Mn of 0.67. Aging did not lead to a strong densification due to sintering. Indeed, a partial preservation of the porous structure appears distinctly. It is remarkable that large Pd particles due to particle sintering are not significantly detected. In contrast, small Pd particles below 2 nm are characterized even though their population is rather low. In parallel, some fluctuations appear on the average La/Mn ratio calculated over all 120 measurements increasing to 0.79 with a narrower dispersion corresponding to a standard deviation of 0.074 vs 0.15 for the calcined sample.

Regarding, calcined Pd/$LaMnO_3$ oxidic Pd species are also well dispersed with PdO particle size ranging from 2 nm to 3 nm. Contrary to Pd/$La_{0.7}MnO_3$, aged Pd/$LaMnO_3$ exhibits larger palladium aggregates either as amorphous hollow particles with size up to 15 nm or as small (1.5 nm) well distributed particles. The quantification of the La/Mn ratio (see Fig. 6) reveals a broader distribution with an apparent maximum near 0.9. Similarly, aging leads to increasing value but for this sample the trend observed seems more accentuated with more La-rich grains.

Finally, the examination of several TEM images on Pd/$LaMn_{1.3}O_3$ revealed a lower density of PdO particles in the volume analyzed than on the two previous samples. Even if it seems difficult to obtain an average particle size, Fig. 5 shows that the size of the PdO particles on Pd/$La_{1.3}MnO_3$ is rather comparable to the two previous calcined samples. After aging, one can observed that palladium aggregates into larger particles. Aging induces more aggregation leading to preferential Pd-rich area showing more heterogeneous Pd distributions compared to Pd/$La_{0.7}MnO_3$ and Pd/$LaMnO_3$. This observation seems in good agreement with the very low

Pd dispersion obtained on this catalyst suggesting possible encapsulation of PdO particles hindering their accessibility in agreement with previous observations on noble metals supported on lanthana [32]. Alternately, the formation of mixed-metal oxides associated to $LaPtO_x$ on Pt/La_2O_3-Al_2O_3 [33] cannot be completely ruled out for on La-rich $Pd/La_{1.3}MnO_3$ catalysts. Fig. 6 shows a distribution quasi-unchanged on calcined and aged samples. The broad distribution on the La/Mn ratio, with two apparent maxima near 1.25 and up to 2, emphasizes a stable La-rich surface.

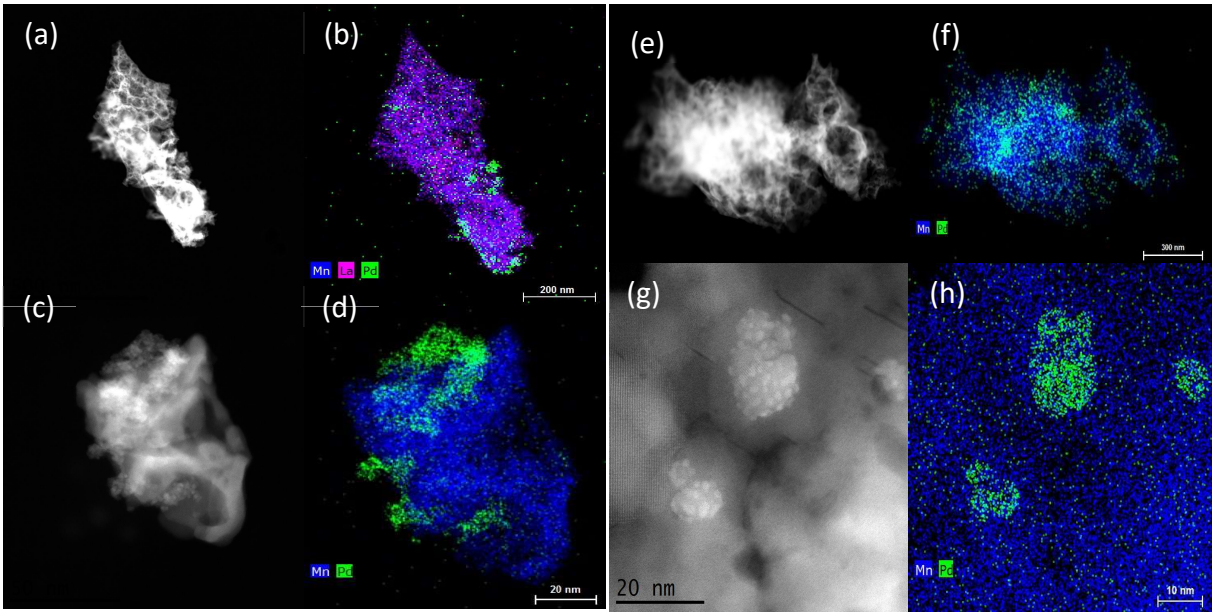

Fig. 3. Characteristic HAADF images at lower and higher magnification and the corresponding STEM-EDS maps for calcined in air at 400°C (a)-(d) and aged (e)-(h) $Pd/La_{0.7}MnO_3$.

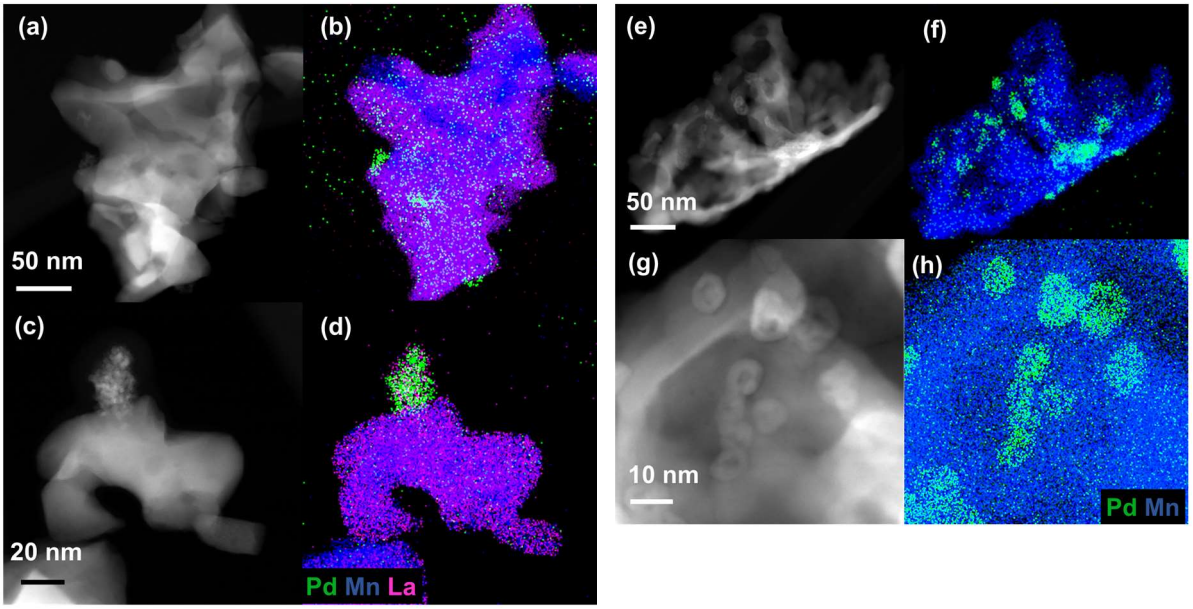

Fig. 4. Characteristic HAADF images at lower and higher magnifications and the corresponding STEM-EDS maps for the calcined in air at 400°C (a)-(d) and aged (e)-(h) Pd/$LaMnO_3$.

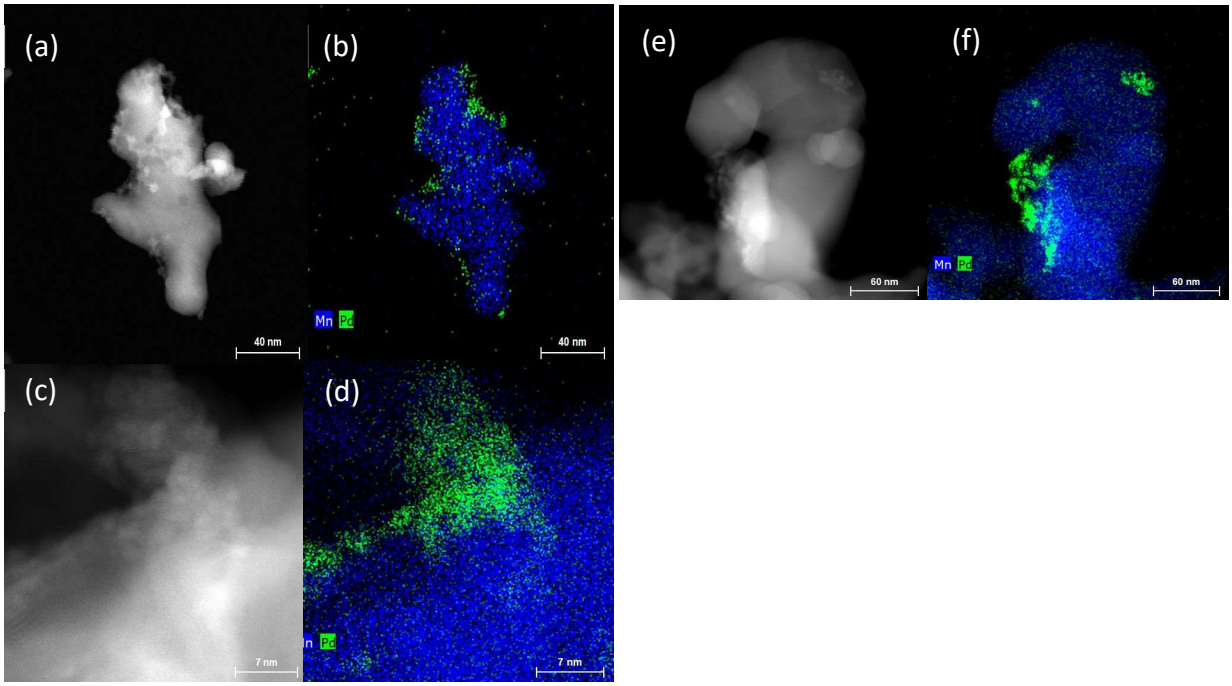

Fig. 5. Characteristic HAADF images at lower and higher magnification and the corresponding STEM-EDS maps for calcined in air at 400°C (a)-(d) and aged (e)-(f) Pd/$La_{1.3}MnO_3$.

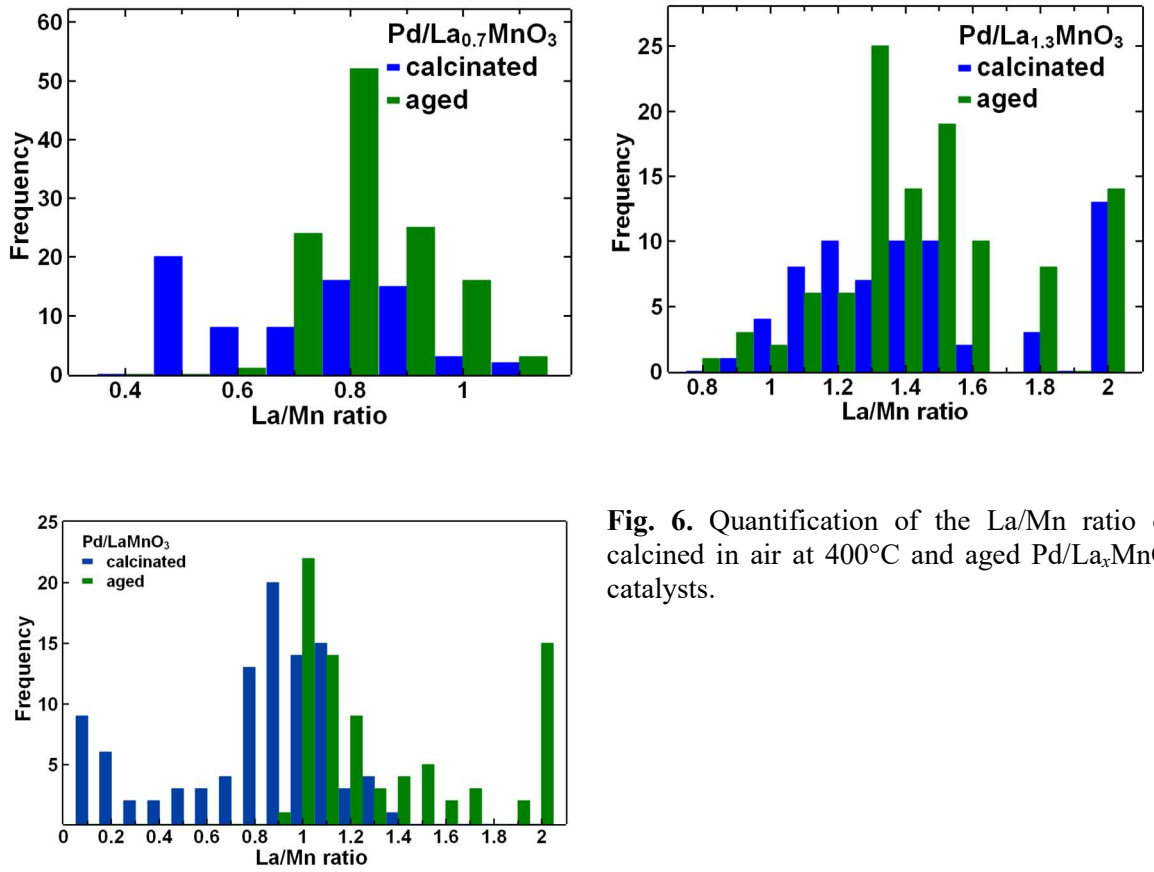

Fig. 6. Quantification of the La/Mn ratio on calcined in air at 400°C and aged Pd/La$_x$MnO$_3$ catalysts.

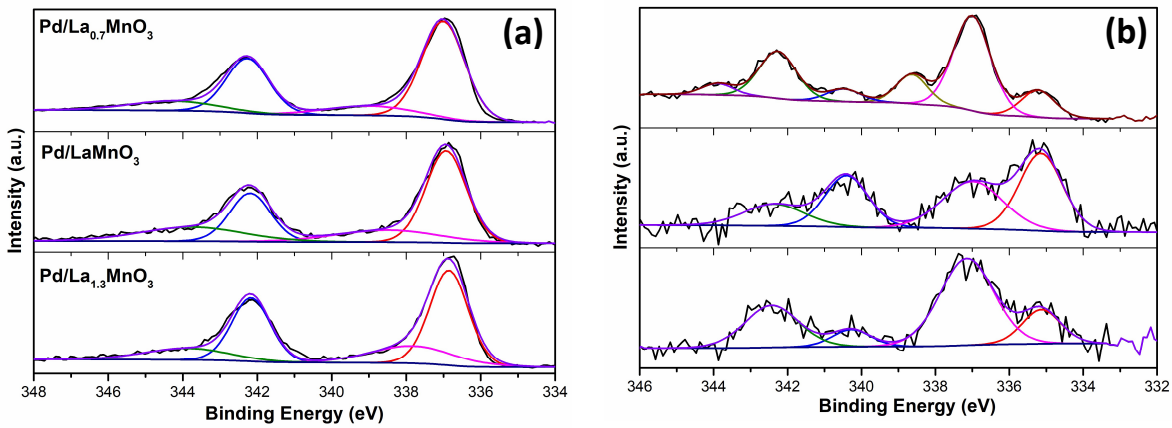

Fig. 7. Pd 3d photopeak from XPS analysis of calcined (a) and aged Pd/La$_x$MnO$_3$ catalysts (b).

Table 2. Physicochemical properties of calcined Pd-doped La_xMnO_3

Catalyst	Specif. Surf. Area (m^2/g)	Pore volume (cm^3/g)	Reducibility [a]		O_2-Temperature-Programmed Desorption			
			Total H_2 uptake (mmol/g)	H/Mn+Pd	α-O_2 desorption (μmol/g)	β-O_2 desorption (μmol/g)	Total desorbed O_2 (μmol/g)	Normalized desorbed O_2 (μmol/m^2)
$Pd/La_{0.7}MnO_3$	28.9	0.20	3.71	1.8	96	531	716	24.8/18.4 [b]
$Pd/LaMnO_3$	20.7	0.14	2.94	1.4	49	522	571	27.6/25.2 [b]
$Pd/La_{1.3}MnO_3$	22.3	0.14	2.65	1.3	69	468	537	24.1/21.0 [b]

[a] from H_2-TPR measurements

[b] calculation taking only β-O_2 desorption

Table 3. Surface characterization of Pd-doped La_xMnO_3 perovskites

Catalyst	Thermal treatment	SSA (m^2/g)	Pd dispersion (%) [a]	Surface XPS composition					
				Mn/La	Pd/La+Mn	$Pd^0/(Pd^{n+}+Pd^{2+})$ [c]	Pd^{n+}/Pd^{2+} [c]	Mn^{4+}/Mn^{3+}	$O_{ads}/O_{lattice}$ [d]
$Pd/La_{0.7}MnO_3$	Calcined	28.9	6.2	1.04/1.4 [b]	0.108	~0	0.25	5.87	1.15
	Aged			1.67/1.4 [b]	0.037	0.25	0.24	1.08	4.66
$Pd/LaMnO_3$	Calcined	20.7	13.0	0.83/1.0 [b]	0.032	~0	0.48	4.79	0.97
	Aged			0.77/1.0 [b]	0.015	1.34	~0	0.69	3.36
$Pd/La_{1.3}MnO_3$	Calcined	22.3	1.0	0.70/0.8 [b]	0.055	~0	0.28	5.47	1.11
	Aged			0.55/0.8 [b]	0.010	0.44	~0	0.88	2.15

[a] from H_2 chemisorption at 100°C on pre-reduced samples at 250°C

[b] bulk atomic ratio

[c] with n>2

[d] O_{ads} accounts for the component at 531 eV and 532.9 eV. $O_{lattice}$ stands for the contribution at 529 eV

3.2.5. Surface XPS analysis

Surface composition was analysed from XPS on calcined and aged samples. The depth analysed by this technique is approximately 50-100 nm which reflect the surface composition for the perovskite while for nanosized Pd particles subsurface layer are considered. Particular attention was paid to La 3d, Mn 2p, O 1s and Pd 3d core levels. Spectral features for La 3d remain unchanged irrespective of La-stoichiometry on calcined and aged samples characterizing trivalent cation La^{3+}. Two major components appear on the O 1s photopeak on calcined samples near 529.0 eV and 531.0 eV (see Fig. S2 in SI) respectively assigned to surface oxygen lattice species ($O_{lattice}$) and adsorbed oxygen species (O_{ads}), *i.e.* O_2^-, O^- or OH groups. A weak and broad contribution near 532.9 eV characterizes the stabilization of carbonate species at the surface on calcined samples. This latter contribution strongly intensifies on aged samples. Their formation can result from the interaction between gaseous CO_2 formed in the course of the reaction with surface OH groups or surface lattice oxygen O_{surf}^{2-} leading respectively to weakly and strongly hydroxy-carbonates and/or carbonates species [34]. This explanation seems consistent with the significant attenuation of the 531.0 eV component. The intensity of 532.9 eV signal has been considered in the O_{ads} component. Hence, a sharp increase of surface O_{ads}-to-$O_{lattice}$ ratio is noticeable on aged samples (see Table 3). Let us note that Mn^{4+} and Mn^{3+} coexist in all calcined samples. A significant decrease of Mn^{4+}/Mn^{3+} ratio is systematically observed on aged catalysts and can be partly explained by the pre-reductive treatment. No clear comparison appears with the more complex evolution observed on the La/Mn ratio. Indeed, aging induces a decrease of this ratio emphasizing Mn-rich surface on aged $Pd/La_{0.7}MnO_3$. In contrast, the reverse trend characterizes $Pd/La_{1.3}MnO_3$ corresponding after aging to La-rich surface. $Pd/LaMnO_3$ exhibits an intermediate behavior as the La/Mn ratio remains quasi-unchanged with variations likely within the margin of error. Let us note that these trends

globally agree with STEM-EDS analysis emphasizing Mn-rich surface on $Pd/La_{0.7}MnO_3$ and La-rich surface on $Pd/La_{1.3}MnO_3$.

Key information lies in the evolution of the oxidation state of palladium and the relative composition. First, Pd^{2+} species are predominantly characterized on calcined catalysts with B.E. values near 337.0 eV. This assignment seems consistent with STEM-EDS analysis revealing the presence of PdO particles. Spectral decomposition of Pd 3d photopeak recorded on aged samples show two extra components. A lower B.E. component grows on aged catalysts near 335.0 eV characteristic of metallic Pd^0 species. This contribution dominates on $Pd/LaMnO_3$ and coincides to an attenuation of the 336.0 eV signal. The presence of metallic Pd species can be reasonably explained by the pre-reductive treatment but aging at 750°C can destabilize PdO enhancing their decomposition to Pd^0. An additional contribution arises near 337.6 eV on aged $Pd/LaMnO_3$ and $Pd/La_{1.3}MnO_3$, significantly shifted to higher B.E. value on $Pd/La_{0.7}MnO_3$ at 338.6 eV, associated to an increase of the oxidation state of Pd^{n+} with $n > 2$ and/or the redistribution of oxidic palladium species in specific coordination with the surface of the perovskite [35,36]. Let us note that the shift observed on aged $Pd/La_{0.7}MnO_3$ coincides with surface Mn enrichment. In contrast, the Mn/La ratio for $Pd/LaMnO_3$ and $Pd/La_{1.3}MnO_3$ evidences La-rich surfaces, this trend being more accentuated on aged $Pd/La_{1.3}MnO_3$. These surface changes in terms of surface composition and oxidation state underline the fact that several types of interactions can occur between Pd and the support materials depending on the stoichiometry of La and the importance of the surface reconstructions operating during thermal aging.

4. Discussion

As displayed in the introduction, La-stoichiometry can modify substantially the surface properties of the perovskite and related strength of interaction with nanosized palladium particles. Indeed, improved oxygen mobility and a greater concentration of surface anionic vacancies can stabilize palladium entities at high temperature [8]. The kinetics of the CH_4/O_2 reaction has been studied on pre-reduced catalysts. Previous study of the CH_4/O_2 reaction on pre-reduced $Pd/La_{0.7}MnO_3$ catalyst led to a mechanism proposal involving a dual site in scheme 1(b) combining metallic Pd species and surface reactive oxygen species from the support. A first objective in this study was to extend the validity of this previous conclusion to various lanthanum-stoichiometries and verify if this dual reaction mechanism is enough robust to explain the changes observed on the kinetic features reported in Table 1 on pre-reduced and aged samples.

As illustrated, the experimental specific reaction rates are of the same order of magnitude irrespective of the La-stoichiometry on pre-reduced samples. A strong inhibiting effect of water is equally observed on pre-reduced and aged catalysts. Reaction rates on pre-reduced and aged samples recorded in dry conditions remains unchanged on $Pd/La_{0.7}MnO_3$ and slightly decrease on $Pd/LaMnO_3$. In fact, $Pd/La_{1.3}MnO_3$ seems to be the most sensitive to deactivation effects induced by the thermal aging at 750°C. The comparison of the pre-exponential factor A, and of the apparent activation energy E_{app} of the rate constant k on Pd/La_xMnO_3 reveals different evolutions. Indeed, a compensation effect is observed on $Pd/La_{0.7}MnO_3$ and $Pd/LaMnO_3$ with a joint decrease of A and E_{app} on aged samples. In contrast, these two parameters remain of the same order of magnitude on pre-reduced and aged $Pd/La_{1.3}MnO_3$ catalysts with only weak variations likely within the margin of error. Hence, a first question arises relative from these evolutions and if they can be reconciled according to the same reaction mechanism. A second

question is related to the existing relationship between changes in catalytic features and surface properties driven by physicochemical processes taking place during aging.

4.1. Nature and evolution of the Pd-$LaMnO_3$ interface during thermal aging.

Calcination of La_xMnO_3 led to bulk detectable impurities with Mn_2O_3 and La_2O_3 segregations which accentuate for x = 0.7 and 1.3 respectively. On the other hand, the specific surface areas are of the same order of magnitude in the range 21-29 m^2/g which cannot explain the change observed on the palladium dispersion determined from H_2 titration varying from 1.0% on $Pd/La_{1.3}MnO_3$ to 13.0% on Pd/MnO_3. Prior reaction the catalysts are pre-reduced at 250°C in similar conditions to stabilize metallic Pd particles. It was checked that the perovskite structure did not deteriorate inducing loss of their intrinsic redox properties [21]. Indeed, extensive reduction to La_2O_3 and MnO occurs above 500°C [37]. The weak evolution on the reaction rates on pre-reduced are not compatible to the strong changes observed on metallic Pd dispersion especially on $Pd/La_{1.3}MnO_3$. This disagreement suggests the potential role that the perovskite support could play. Based on this, the La/Mn ratio could be a relevant descriptor as noticeable changes occur on aged catalysts and reveal divergent evolutions. Indeed, exposure to 750°C in wet conditions (10 vol.% H_2O in 5 vol.% O_2) leads to Mn-rich surface on $Pd/La_{0.7}MnO_3$ and La-rich surface on $Pd/La_{1.3}MnO_3$ as evidenced from XPS analysis and globally from STEM-EDS analysis. The presence of surface metallic palladium species is confirmed from XPS but oxidic Pd^{n+} palladium species are also detected which correspond to a higher oxidation state than Pd^{2+} predominating on calcined samples. The stabilization of palladium ad-atoms in unusual oxidation characterized by and oxidation state higher than +2 or in strong interaction with the support have been earlier reported [38,39]. There stabilization is closely related to the nature of the support and would reflect a closer proximity between cationic

palladium species and oxygen species from the support [40]. Interestingly, Pd^{n+} species are still detected on aged $Pd/La_{0.7}MnO_3$ but completely disappear on aged $Pd/LaMnO_3$ and $Pd/La_{1.3}MnO_3$ emphasizing their greater instability to thermal aging which could suggest a more resistant Pd-support interface on $Pd/La_{0.7}MnO_3$. This highlights important structural changes during aging stabilizing palladium in unusual oxidation state especially on $Pd/La_{0.7}MnO_3$. It should also be noted that the Mn^{4+}/Mn^{3+} ratio on the calcined samples is systematically reduced on the aged catalysts. This trend does not coincide with the evolution of the La/Mn ratio and could be more consistent with an important reduction of Mn^{4+} in the perovskite network to Mn^{3+} during the pre-reduction treatment. HAADF-STEM analysis did not emphasize strong evolution of the palladium particle size on calcined and aged samples. Particle sintering occurs moderately as large aggregates have not been detected in number. However, it seems obvious that the density of palladium particles detected slightly reduce on aged samples. To summarize changes in the surface Mn concentration should modify the palladium interface. Indeed, contrarily to La^{3+} manganese is characterized by a mixed valence which govern oxygen storage properties. Hence, for x = 0.7 and 1.3, Mn-rich and La-rich surface should lead to different types of interface with palladium governing their catalytic properties. As thermal aging accentuates the difference observed on calcined samples, then some evolutions on the kinetics of the CH_4/O_2 reaction would be expected.

4.2. Single site vs. dual sites reaction mechanism on pre-reduced and aged Pd/La_xMnO_3 catalysts.

The mathematical expressions of the reaction rates corresponding to the two reaction mechanisms in scheme 1 can be established assuming the first C-H bond scission (steps 3(a) and 3(b)) in adsorbed methane molecules as limiting steps [6]. By considering all the other steps

fast, then reversible steps can be assumed quasi-equilibrated. This means that methane and oxygen adsorptions can be considered quasi at equilibrium which makes easier the determination of corresponding expressions for the surface coverage of O atoms and CH_4 molecules adsorbed on palladium, *i.e.* θ_O^* and $\theta_{CH_4}^*$, according to Eqs. (12) and (13). A second hypothesis accounts for O_{ads} and $CH_{4,ads}$ as the most abundant adsorbed species at the surface which ease the derivation of the expression of the fraction of vacant site given by Eq. (14).

$$\theta_O^* = \sqrt{\mathrm{K_O P_{O_2}}}\,\theta_v^* \quad (12)$$

$$\theta_{CH_4}^* = \mathrm{K}_{CH_4}\mathrm{P_{CH_4}}\,\theta_v^* \quad (13)$$

$$\text{with } \theta_v^* = \frac{1}{1+\mathrm{K}_{CH_4}\mathrm{P_{CH_4}}+\sqrt{\mathrm{K_O P_{O_2}}}} \quad (14)$$

Hence, the reaction rate expression for the single site reaction mechanism can be expressed from step (3a). This example illustrates the potential assistance of O_{ads} species to ease the C-H bond breaking. The substitution of θ_O^*, $\theta_{CH_4}^*$ and θ_v^* by their expression in Eqs. (12)-(14) leads to Eqs. (15) where k_{3a} stands for the rate constant for step (3a), K_{CH_4} and $\mathrm{K_O}$ the equilibrium constant for CH_4 and O_2 adsorption, $p(CH_4)$ and $p(O_2)$ the partial pressures of CH_4 and O_2 respectively.

$$r_{3a} = k_{3a}\theta_{CH_4}^*\theta_O^* = \frac{k_{3a}K_{CH_4}p(CH_4)\sqrt{\mathrm{K_O}p(O_2)}}{\left[1+\mathrm{K}_{CH_4}p(CH_4)+\sqrt{\mathrm{K_O}p(O_2)}\right]^2} \quad (15)$$

For the dual-site mechanism, the corresponding reaction rate is given by Eq. (16) where θ_O stands for the fraction of surface reactive oxygen species supplied by the support at the vicinity of adsorbed CH_4 molecules on Pd sites.

$$r_{3b} = k_{3b}\theta_{CH_4}^*\theta_O \quad (16),$$

'O' and 'OH' species have been assumed as the most abundant species at the surface of the perovskite support in large excess of gaseous oxygen leading to Eq. (17). The expression of θ_O can be obtained by solving steady-state Eq. (18). Consecutive rearrangements finally lead to Eq. (19).

$$\theta_O + \theta_{OH} \approx 1 \quad (17)$$

$$\frac{d\theta_{OH}}{dt} = 4r_{3b} - r_{10} = 4k_{3b}\theta^*_{CH_4}\theta_O - k_{10}\theta^2_{OH} = 0 \quad (18)$$

$$r_{3b} = \frac{k_{3b}K_{CH_4}p(CH_4)}{(1+K_{CH_4}p(CH_4)+\sqrt{K_O p(O_2)})}\left[1 + \frac{2k_{3b}K_{CH_4}p(CH_4)}{k_{10}(1+K_{CH_4}p(CH_4)+\sqrt{K_O p(O_2)})}\right] \quad (19)$$

Kinetic and thermodynamic parameters, *i.e.* k_n, K_{CH_4} and K_O have been estimated from a least square method consisting in minimizing the sum of the square difference between predicted and experimental reaction rates $\sum(r_{exp.} - r_{predic.})^2$. Predicted reaction rates have been adjusted taking equally the participation of both reaction mechanisms in scheme 1 into account, *i.e.* $r_{predic.} = r_{3a} + r_{3b}$. The adjusted values of the rate constants and the equilibrium constants for adsorption from this adjustment routine are collected in Table 2. The contribution of the dual-site reaction mechanism on $r_{predic.}$ can be estimated from the optimized K and *k* values. First on pre-reduced catalysts, the dual-site reaction mechanism prevails on $Pd/La_{0.7}MnO_3$ and $Pd/LaMnO_3$ whereas the single-site reaction mechanism, by considering active sites only composed of palladium, predominates on $Pd/La_{1.3}MnO_3$. After aging, the kinetics of the CH_4/O_2 reaction on aged $Pd/La_{0.7}MnO_3$ is still governed only by the dual-site catalysts while the contribution of both mechanisms becomes more equilibrated on aged $Pd/LaMnO_3$ which would reflect changes in the nature of the Pd-support interface. Partial deterioration could be related to particle sintering observed from TEM analysis. It also appears that the characterization of surface cationic Pd^{n+} species from XPS analysis could be a good descriptor to probe the evolution of the Pd-La_xMnO_3 interface. Their stabilization on $Pd/La_{0.7}MnO_3$ and their disappearance on $Pd/LaMnO_3$ and $Pd/La_{1.3}MnO_3$ seem in good agreement with the preservation of the dual-site reaction mechanism on $Pd/La_{0.7}MnO_3$ while its

contribution lowers on $Pd/LaMnO_3$. Interestingly the trend observed on the kinetics on $Pd/La_{1.3}MnO_3$ becomes more pronounced as the CH_4/O_2 reaction only obeys to single site reaction mechanism on aged sample. This seems consistent to a more La-rich surface reducing the interaction between palladium and manganese.

4.3. Comparison with theoretical insights.

Theoretical data have been previously obtained from the unity bond index-quadratic exponential potential (UBI-QEP) method [41]. This is a thermodynamic approach which allows straightforward calculations of heat and activation barriers of elementary steps. Results previously obtained on a closed-packed Pd (111) surface with preferred three-fold hollow sites [21] have been complemented by integrating the influence of the surface coverage of the adsorbates. Based on this, possible comparisons can be expected based on the estimated O-coverage calculated on $Pd/La_{1.3}MnO_3$ obeying quasi-exclusively to a single site mechanism. As previously explained, some restrictions must be considered because the UBI-QEP model cannot include in the modeling attractive and repulsive interactions between two different adsorbates. Based on this, the influence of O- and OH-coverages on the activation energy of step (3a), *i.e.* $CH_{4*} + O* \leftrightarrows CH_{3*} + OH*$, accounts for the interactions between two O atoms or two OH groups but neglects possible interactions between O and OH adsorbates. Thus, the plot $Ef(\theta)$ versus θ_O and θ_{OH} can be obtained revealing a decrease of the activation barrier when θ_O exceed 40% (see Fig. 8). In contrast, the accumulation at the surface of OH group has a detrimental effect increasing the activation barrier.

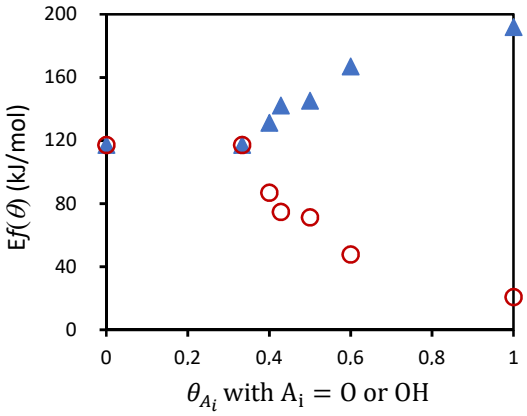

Fig. 8. Surface oxygen and OH coverage dependency of activation barrier of step (3b) (▲) O coverage (○) and OH coverage Reproduced with permission from ref. [21].

Oxygen and methane coverages can be roughly calculated on Pd/La$_x$MnO$_3$ from Eqs. (12)-(14) by using optimized equilibrium adsorption constants for oxygen and methane in Table 4 for a reaction temperature of 400°C. Let us note that these calculations are not restricted to Pd/La$_{1.3}$MnO$_3$ but can be extended to the two other catalysts samples, the residual θ_O only depending on the competition for adsorption between O_2 and CH_4 on palladium sites. The most prominent observation lies in the order of magnitude of θ_O below the theoretical value of 40% on Pd/La$_{0.7}$MnO$_3$ and Pd/LaMnO$_3$ and up to 80% on Pd/La$_{1.3}$MnO$_3$. Based on this comparison, the high oxygen coverages on Pd/La$_{1.3}$MnO$_3$ are compatible with a significant decrease of the activation barrier which would shift more with reaction mechanism in scheme 1(a) where reaction steps only involved Pd particles. On the other hand, the lower θ_O calculated for Pd/La$_{0.7}$MnO$_3$ and Pd/LaMnO$_3$ do not allow to consider a decrease in the activation barrier. For these two latter catalysts, it seems more plausible to consider the involvement of surface reactive oxygen supplied by the perovskite support as demonstrated from kinetic measurements.

Finally, an important kinetic feature emphasized in Fig. 8 is related to the detrimental effect of OH accumulation onto Pd particles on the kinetics. Indeed, a gradual increase of the activation barrier appears with a rise in OH-coverage predicted by the UBI-QEP method. This prediction is interesting because it suggests that the deleterious effect of OH group accumulation would be equally governed by thermodynamic factors, related to stronger OH

adsorption displacing adsorbed O and CH_4 intermediates, and kinetic factors with increase of the activation barrier reflecting a loss of reactivity of key reaction intermediates. This effect probably is more accentuated in wet conditions in the presence of 0.1 atm H_2O and matches with the trend reported in Table 1. In wet conditions, the growth of $Pd(OH)_2$ at the surface of PdO could induce deactivation in methane oxidation [27]. The combination of unfavourable kinetic and thermodynamic factors limiting the accessibility to the palladium sites and deactivating the intermediates formed should therefore manifest itself more significantly on $Pd/La_{1.3}MnO_3$. The comparisons of the reaction rates recorded in dry and wet conditions in Table 1 seem in agreement and also show that this detrimental effect concerns also $Pd/La_{0.7}MnO_3$ and $Pd/LaMnO_3$ for which the kinetics is governned by the Pd-La_xMnO_3 interface. Previous explanations given on $Pd/La_{0.7}MnO_3$ was related to a partial suppression of the Pd-$LaMnO_3$ interface due to strong accumulation of water blocking oxygen mobility [42]. Similar explanations were also given on Si-doped Pd/CeO_2 catalyst with strong accumulation of stable hydroxyls onto the support hindering oxygen exchange [43]. In the particular case of $Pd/La_{1.3}MnO_3$ this detrimental effect should occur in lesser extent as only Pd atoms compose the active sites and lanthanum exhibits poorer oxygen mobility than manganese.

Table 4. Optimized kinetic and thermodynamic parameters on Pd-doped perovskite based catalysts for CH_4 combustion

Catalyst	Thermal treatment	k_{3b} [b]	k_{3a} [b]	k_{10} [b]	K_{CH_4} [c]	K_{O_2} [c]	Contribution mech. 1(b) (%)
$Pd/La_{0.7}MnO_3$	Pre-red. [a]	2.5×10^{-6}	0	0.05	17.2	0.05	100
	Aged	11.6×10^{-6}	0	0.02	5.7	0.08	100
$Pd/LaMnO_3$	Pre-red. [a]	2.2×10^{-5}	4.6×10^{-5}	0.61	164	0.05	83
	Aged	3.1×10^{-5}	8.5×10^{-5}	0.71	65	1.50	53
$Pd/La_{1.3}MnO_3$	Pre-red. [a]	3.5×10^{-4}	2.0×10^{-3}	0.50	5.1	391	17
	Aged	1.1×10^{-5}	3.5×10^{-5}	0.51	3.9	430	0

[a] prereduced at 250°C in pure H_2
[b] mol/min/g
[c] atm^{-1}

5. Conclusion

This study reports important kinetic features for the catalytic CH_4/O_2 reaction on 1 wt.% Pd/La_xMnO_3. This reaction has a practical interest with the emergence of Compressed-Natural-Gas engines less harmful towards atmospheric environment but the abatement of methane leakage must be avoided and need the implementation of efficient and robust catalytic-after -treatment systems.

Particular attention was paid in this study to the influence of the Pd-La_xMnO_3 interface taking various La-compositions with x = 0.7, 1.0 and 1.3 into account. Steady-state kinetic measurements have been performed in lean conditions at 400°C on pre-reduced and on aged catalysts after exposure to 10 vol.% H_2O with 5 vol.% O_2 diluted in He at 750°C. Kinetic data have been compared to two different reaction mechanisms: *(i)* a single-site reaction mechanism, which accounts for active sites only composed of Pd, and *(ii)* a dual-site reaction mechanism combining Pd and surface reactive oxygen species. For 1 wt.% Pd/$La_{1.3}MnO_3$, Pd interacts mostly with La having weak oxygen mobility. Hence, the single-site reaction mechanism prevails and this trend accentuates after aging. In contrast, the dual-site reaction mechanism only occurs on pre-reduced and aged Pd/$La_{0.7}MnO_3$ reflecting a strong Pd-support interface. Pd-$LaMnO_3$ exhibits an intermediate kinetic behaviour with the coexistence of both mechanisms. Let us note that the contribution of the single site reaction mechanism increases after aging emphasizing a deterioration of the Pd-La_xMnO_3 interface. SEM-HAADF and XPS measurements clearly shows that the driving force is related to the interaction between Mn and Pd which increases on aged Pd/$La_{0.7}MnO_3$ while a decrease is noticeable on aged Pd/$La_{0.7}MnO_3$ and Pd/$LaMnO_3$. The presence of Pd^{n+} species can be also considered as a descriptor to probe the interface. Indeed, their surface concentration remains unchanged on aged Pd/$La_{0.7}MnO_3$ while less stable Pd^{n+} species on Pd/$La_{1.3}MnO_3$ and Pd/$LaMnO_3$ disappear after aging. On this

basis, Pd/$La_{0.7}MnO_3$ exhibits the best compromise in terms of catalytic properties and thermal stability.

Finally, this study provides useful kinetic information in connection with the surface composition of Pd-based CNG catalysts. This could offer new guidelines in optimizing their design. Accordingly, a possible reduction of PGM loading could be envisioned keeping high catalytic performances.

Acknowledgements

This work was financially supported by the French National Research Agency through the project ANR-18-CE07-0040. One of the co-authors (Y. Zheng) was able to benefit from a thesis grant within the framework of this program. The REALCAT platform was funded by the French National Research Agency (ANR-11-EQPX-0037) within the frame of the 'Future Investments' program (PIA). The Nord-Pas-de-Calais Region and the FEDER are acknowledged for their financial contribution to the equipment of the platform.

Reference

[1] L.G. Andersson, Effect of using renewable fuels on vehicles emissions, Renewable sustainable Energy Rev. 47 (2015) 162-172. https://doi.org/10.1016/j.rser.2015.03.011.

[2] P. Granger, Challenges and breakthroughs in post-combustion catalysis: how to match future stringent regulations, Catal. Sci. Technol. 7 (2017) 5195-5211. https://doi.org/10.1039/C7CY00983F.

[3] A. Raj, Methane Emission Control, Johnson Matthey Technol. Rev. 60 (2016) 228-235. https://doi: 10.1595/205651316X692554.

[4] H.Q. Robert F. Hicks, Michael L.Young, Raymond G.Lee, Structure Sensitivity of Methane Oxidation over Platinum and Pd, J. Catal. 122 (1990) 280-294. https://doi.org/10.1016/0021-9517(90)90282-O.

[5] A.Y. Stakheev, A.M. Batkin, N.S. Teleguina, G.O. Bragina, V.I. Zaikovsky, I.P. Prosvirin, A.K. Khudorozhkov, V.I. Bukhtiyarov, Particle Size Effect on CH_4 Oxidation Over Noble Metals: Comparison of Pt and Pd Catalysts, Top. Catal. 56 (2013) 306-310. https://doi.org/10.1007/s11244-013-9971-y.

[6] K.-I. Fujimoto, F.H. Ribeiro, M. Avalos-Borja, E. Iglesia, Structure and reactivity of PdO_x/ZrO_2Catalysts for methane oxidation at low temperatures, J. Catal. 179 (1998) 431-442. https://doi.org/10.1006/jcat.1998.2178.

[7] Y. Yoshida, T. Nakajima, Y. Yazawa, T . Hattori, Support effect on methane combustion over palladium catalysts, Appl. Catal. B 71 (2007) 70-79. http://dx.doi.org/10.1016/j.apcatb.2006.08.010.

[8] A. Toso, S. Colussi, S. Padigapaty, C. de Leitenburg, A. Trovarelli, High stability and activity of solution combustion synthesized Pd-based catalysts for methane combustion in presence of water, Appl. Catal. B 230 (2018) 237-245. https://doi.org/10.1016/j.apcatb.2018.02.049.

[9] K.-I. Fujimoto, F.H. Ribeiro, M. Avalos-Borja, E. Iglesia, Structure and Reactivity of PdO_x/ZrO_2Catalysts for Methane Oxidation at Low Temperatures, J. Catal. 179 (1998) 431-442. https://doi.org/10.1006/jcat.1998.2178.

[10] J. Au-Yeung, K. Chen, A.T. Bell, E. Iglesia, Isotopic Studies of Methane Oxidation Pathways on PdO Catalysts, J. Catal. 188 (1999) 132-139. https://doi.org/10.1006/jcat.1999.2643

[11] M. Van de Bossche, H. Grönbeck, Methane Oxidation over PdO(101) Revealed by First-Principles Kinetic Modeling, J. Am. Chem. Soc. 137 (2015) 12035-12044. https://doi.org/10.1021/jacs.5b06069.

[12] H. Stolz, L. Maier, A. Boubnov, A.T. Gremminger, J.D. Grundwaldt, O. Deutschmann, Surface reaction kinetics of methane oxidation over PdO, J. Catal. 370 (2019) 152-175. https://doi.org/10.1016/j.jcat.2018.12.007.

[13] J. Chen, Y. Wu, W. Hu, P. Qu, G. Zhang, P. Granger, L. Zhong, Y. Chen, New insights into the role of Pd-Ce interface for methane activation on monolithic supported Pd catalysts: A step forward the development of novel PGM three-way catalyst for natural gas fueled engine, Appl. Catal. B 264 (2020) N°118475. https://doi.org/10.1016/j.apcatb.2019.118475.

[14] M. Pilar González-Marcos B. Pereda-Ayo, A. Aranzabal, J.A. González-Marcos, J.R. González-Velasco, On the effect of reduction and ageing on the TWC activity of $Pd/Ce_{0.68}Zr_{0.32}O_2$ under simulated automotive exhaust, Catal. Today 180 (2012) 88-95. https:// doi.org/10.1016/j.cattod.2011.04.035.

[15] Y. Lu, K.A. Michalow, S. Kumar Matam, A. Winkler, A.E. Maegli, S. Yoon, A. Heel, A. Weidenkaff, D. Ferri, Methane abatement under stoichiometric conditions on perovskite-supported palladium catalysts prepared by flame spray synthesis, Appl. Catal. B 144 (2014) 631–643. https://doi.org/10.1016/j.apcatb.2013.08.001.

[16] M. Alifanti, J. Kirchnerova, B. Delmon, D. Klvana, Methane and propane combustion over lanthanum transition-metal perovskites: Role of oxygen mobility, Appl. Catal. A. 262 (2004) 167-176. https://doi.org/10.1016/j.apcata.2003.11.024.

[17] R. Spinicci, A. Delmastro, S. Rochetti, A. Tofanari, Catalytic behaviour of stoichiometric and non-stoichiometric $LaMnO_3$ perovskite towards methane combustion, Mater. Chem. Phys. 78 (2002) 393-399. https://doi.org/10.1016/S0254-0584(02)00218-3.

[18] P. Esmaeilnejad-Ahranjani, A. Khodadadi, H. Ziaei-Azad, Y. Mortazavi, Effects of excess manganese in lanthanum manganite perovskite on lowering oxidation light-off temperature for automotive exhaust gas pollutants, Chem. Eng. J. 169 (2011) 282-289. https://doi.org/10.1016/j.cej.2011.02.062.

[19] J. Chen, M. Shen, X. Wang, G. Qi, J. Wang, W. Li, The influence of nonstoichiometry on $LaMnO_3$ perovskite for catalytic NO oxidation, Appl. Catal. B 134–135 (2013) 251–257. https://doi.org/10.1016/j.apcatb.2013.01.027.

[20] Jon A. Onrubia-Calvo, B. Pereda-Ayo, U. De-La-Torre, Juan R. González-Velasco, Key factors in Sr-doped $LaBO_3$ (B = Co or Mn) perovskites for NO oxidation in efficient diesel exhaust purification, Appl. Catal. B 213 (2017) 198–210. https://doi.org/10.1016/j.apcatb.2017.04.068.

[21] Y. Zheng, A. Decoster, A. Osti, A. Glisenti, J.P. Dacquin, F. Dhainaut, S. Heyte, P. Granger, Combined theoretical and experimental kinetic approach for methane conversion on model supported $Pd/La_{0.7}MnO_3$ NGV catalyst : Sensitivity on inlet gas composition and consequence on the Pd-support interface, Appl. Catal. A 641 (2022) 118687. https://doi.org/10.1016/j.apcata.2022.118687.

[22] A.A. Vedyagin, A.M. Volodin, R.M. Kenzhin, V.O. Stoyanovskii, V.E. Rogov, V.V. Kriventsov,I.V. Miskatov, The role of chemisorbed water and stabilization of actives sites on Pd/Alumina oxidation catalysts, Catalysis Today 307 (2018) 102-110. https//doi.org/10.1016/j.cattod.2017.01.033.

[23] Taguchi, S.I. Matsu-ura, M. Nagao, T. Choso, K. Tabata, Synthesis of $LaMnO_{3+\delta}$ by Firing Gels Using Citric Acid, J. Solid State Chem. 129 (1997) 60–65. https://doi.org/10.1006/jssc.1996.7229.

[24] R.S. Monteiro, D. Zemlyanov, J.M. Storey, F.H. Ribeiro, Turnover rate and reaction orders for the complete oxidation of methane on a palladium foil in excess dioxygen, J. Catal. 199 (2001) 291-301. https://doi.org/10.1006/jcat.2001.3176.

[25] G. Zhu, J. Han, . D.Y. Zemlyanov, F. Ribeiro, Temperature dependence of the kinetics for the complete oxydation of methane on palladium and palladium oxide, J. Phys. Chem. B 109 (2005) 2331-2337. https://doi.org/10.1021/jp0488665.

[26] A. Wold, R. Arnott, Preparation and crystallographic properties of the systems $LaMn_{1-x}Mn_xO_{3+\lambda}$ and $LaMn_{1-x}Ni_xO_{3+\lambda}$, J. Phys. Chem. Solids 9 (1959) 176-180. https://doi.org/10.1016/0022-3697(59)90207-0.

[27] F.H. Ribeiro, M. Chow, R.A. Della Betta, Kinetics of the complete oxidation of methane over supported palladium catalysts, J. Catal. 146 (1994) 537-544. https://doi.org/10.1006/jcat.1994.1092.

[28] G. Ertl, P. Rau, P. Chemisorption und katalische reaction von sauerstaff und kohlenmonoxid an einer palladium (110)-oberfläche, Surf. Sci. 15 (1969) 443-465. https://doi-org.inc.bib.cnrs.fr/10.1016/0039-6028(69)90134-4.

[29] Y.D. Zhao, J. Park, R.-J. Jung, H.-J. Noh, S.-J. Oh, Structure, magnetic and transport properties of $La_{1-x}Bi_xMnO_3$, J. Magn. Magn. Mater. 280 (2004) 404-411. https://doi.org/10.1016/j.jmmm.2004.06.024.

[30 P. Norby, I.G.K. Andersen, E.K. Andersen, N.H. Andersen, The crystal structure of lanthanum manganate(iii), $LaMnO_3$, at room temperature and at 1273 K under N_2, J. Solid State Chem. 119 (1195) 191-196. https://doi:10.1016/0022-4596(95)80028-N.

[31] L.G. Tejuca, J.L.G. Fierro, J.M.D. Tascón, Structure and reactivity of perovskite-type oxides, Adv. Catal. 36 (1989) 237–328. https://doi.org/10.1016/S0360-0564(08)60019-X.

[32] S. Bernal, F.J. Botana, R. Garcia, J.M. Rodriguez,-Izquierdo, Metal-support interaction phenomena in some high metal loading lanthana supported rhodium catalyst, Stud. Surf. Sci. Catal. 48 (1989) 123-132. http://dx.doi.org/10.1016/S0167-2991(08)60676-X.

[33] J.C.S. Araújo, L.F. Oton, B. Bessa, A.B.S. Neto, A.C. Oliveira, R. Lang, L. Otubo, J.M.C. Bueno, The role of Pt loading on La_2O_3-Al_2O_3 support for methane conversion reactions via partial oxidation and steam reforming, Fuel 254 (2019) 115681. https://doi.org/10.1016/j.fuel.2019.115681.

[34] J.-G. Kang, Y.-I. Kim, D.W. Cho, Y. Sohn, Synthesis and physicochemical properties of $La(OH)_3$ and La_2O_3 nanostructures, Mater. Sci. Sem. Process. 40 (2015) 737-743. https://doi.org/10.1016/j.mssp.2015.07.050.

[35] Y. Liu, Y. Cai, X. Tang, C. Shao, Y. You, L. Wang, W. Zhan, Y. Guo, Y. Zhao, Y. Guo, Insight into the roles of Pd state and CeO_2 property in C_3H_8 catalytic oxidation on Pd/CeO_2, Appl. Surf. Sci. 605 (2022) 154675. https://doi.org/10.1016/j.apsusc.2022.154675.

[36] G. Corro, O. Vazquez-Cuchillo, F. Banuelos, J.L.G. Fierro, M. Azomoza, An XPS evidence of the effect of the electronic state of Pd on CH_4 oxidation on Pd/γ–Al_2O_3 catalysts, Catal. Commun. 8 (2007) 1977–1980. https://doi.org/10.1016/j.catcom.2007.03.020.

[37] G. Guo, K. Lian, F. Gu, D. Han, Three-dimensionally ordered microporous Pd-$LaMnO_3$ self-regeneration catalysts for methane combustion, Chem. Commun. 50 (2014) 13575-13577. https://doi.org/10.1039/C4CC05966B.

[38] A. Boucly, L. Artiglia, M. Roge, M. Zobilskyi, A. Beck, D. Ferri, J.A. Bokhoven, Appl. Surf. Sci. 606 (2022) 154927. https://doi.org/10.1016/j.apsusc.2022.154927.

[39] A.S. Ivanova, E.M. Slavinskaya, R.V. Gulaev, V.I. Zikovskii, O.A. Stonkus, I.G. Danilova, L.M. Plyasova, I.A. Polukhina, A.I. Boronin, Metal-support interactions in Pt/Al_2O_3 and Pd/Al_2O_3 catalysts for CO oxidation, Appl. Catal. B 97 (2010) 57-71. https://doi.org/10.1016/j.apcatb.2010.03.024.

[40] B. Ealet, E. Gillet, Metal-alumina: influence of the oxide stoichiometry studied by EELS and XPS, Surf. Sci. 281 (1993) 91-101. https://doi.org/10.1016/0039-6028(93)90858-H.

[41] E. Shustorovich, A.T. Bell, Decomposition and reduction of NO on transition metal surfaces: bond order conservation Morse potential analysis, Surf. Sci. 289 (1993) 127-138. https://doi.org/10.1016/0039-6028(93)90892-N.
[42] W.R. Shwartz, L.D. Pfefferle, Combustion of Methane over Palladium-Based Catalysts: Support Interactions, J. Phys. Chem C 116 (2012) 8571-8578. https://doi.org/10.1021/jp2119668.
[43] A. Toso, S. Colussi, J. Llorca, A. Trovarelli, The dynamics of PdO-Pd phase transformation in the presence of water over Si-doped Pd/CeO_2 methane oxidation catalysts, Appl. Catal. A 574 (2019) 79-86. https://doi.org/10.1016/j.apcata.2019.01.023